Characterization of silicon nanowire by use of full-vectorial finite element method

N. Kejalakshmy, Arti Agrawal, Yasin Aden, D. M. H. Leung, B. M. A. Rahman,* and K. T. V. Grattan

School of Engineering and Mathematical Sciences, Northampton Square, London EC1V 0HB, UK

*Corresponding author: B.M.A.Rahman@city.ac.uk

Received 5 January 2010; revised 11 April 2010; accepted 7 May 2010; posted 11 May 2010 (Doc. ID 121958); published 31 May 2010

We have carried out a rigorous **H**-field-based full-vectorial modal analysis and used it to characterize, more accurately, the abrupt dielectric discontinuity of a high index contrast optical waveguide. The full-vectorial **H** and **E** fields and the Poynting vector profiles are described in detail. It has been shown through this work that the mode profile of a circular silicon nanowire is not circular and also contains a strong axial field component. The single-mode operation, vector field profiles, modal hybridness, modal ellipticity, and group velocity dispersion of this silicon nanowire are also presented. © 2010 Optical Society of America

OCIS codes: 060.2310, 230.7370.

1. Introduction

When the waveguide dimension of an optical device is much smaller than the operating wavelength, unique material and structurally dependent properties are evident, and these have attracted much attention recently. Among the variety of materials considered so far, silicon has been particularly attractive, as the low-cost and mature fabrication technology familiar in the electronics domain can then be exploited. Its high index contrast results a tight confinement, allowing efficient scaling and close packing of photonic components. In waveguiding applications, the small size of the silicon core with the silica cladding has allowed the fabrication of quantum wire [1]. Recently the high index contrast in devices with a silicon core and silica or air cladding (for use at visible wavelengths) has allowed the initiation of a number of studies in the silicon photonics field [2]. As a result, it is expected that high speed opto-electronic silicon-based technology would be a candidate for ultra-high-speed communications systems [3], slow light devices [4], atom trapping [5], sensing [6], optical computing [7] and the exploitation of radiation pressure to actuate nanomechanical devices [8]. It is also reported that in the subwavelength regime, the size of the waveguide becomes crucial in the determination of the dispersion properties. Besides, taking advantage of high optical intensities coupled with carefully engineered group-velocity-dispersion (GVD) characteristics, silicon waveguides have been designed by adjusting the silicon cross section for various nonlinear applications, such as Raman amplification, four-wave mixing, and supercontinuum generation [9–12].

In this article, a cylindrical nanowire composed of a silicon core with a silica cladding has been numerically characterized to reveal some of the interesting features of these nanowaveguides. To characterize such a high index contrast optical waveguide in the submicron scale, a rigorous full-vectorial finite element method [13] is used in this study. It is reported here that the modal field profile of a circular nanowire with a subwavelength core radius is not circularly symmetric, with large nondominant transverse and axial field components and for this type of structure, a scalar field or 1-dimensional approach

0003-6935/10/163173-09$15.00/0

would not be valid. The total modal dispersion of such a structure and the dispersion features have been analyzed and results reported.

2. Result

A. Modal Characteristics

Optical nanowire can be fabricated either by physical drawing [14–17] or by chemical reaction [1] for a variety of materials, including high-index silicon. In this work, a circular geometry nanowire [18] with a silicon core of radius R has been investigated, with a silica cladding. The refractive indices of the core and cladding have been considered for $\lambda = 1.55\ \mu$m as $n_{\text{core}} = 3.4754$ and $n_{\text{clad}} = 1.444$ [9,19], respectively. Although the structure has circular symmetry, this is not imposed, but the available twofold mirror symmetry has been exploited. Depending on the modes being investigated, various combinations of the electric or magnetic wall boundary conditions along the X and Y axes have been considered. In the simulation, the quarter-waveguide is represented by nearly 80,000 first-order triangles. The area of the triangles vary over the range 0.2–0.00001 μm^2, with a higher mesh density in the core area. The highly sparse eigenvalue equation [13] containing more than 121,000 unknown variables was solved on a Linux platform (Intel Core Duo processor T2600) in 19 s for each of the modes.

Vector notation, such as EH_{mn} or HE_{mn}, is used to describe the modes of optical waveguides, where the axial E_z or axial H_z field is nonzero. In the special case of weak guidance, the axial field component (E_z or H_z) vanishes and the modes of the waveguide are transverse in nature, and in circular waveguides such as fibers, these modes can have arbitrary transverse polarization. Usually two independent sets of x- and y-polarized modes that have the same propagation constant are assumed. The nomenclature often used is the LP_{mn} notation, where m and n identify the mode orders in the azimuthal and radial directions, respectively. LP_{mn} modes have either a dominant H_x or H_y field. The modes with the dominant H_x and E_y (or H_y and E_x) fields are classified as y-polarized (or x-polarized) modes. In the work presented here, although the silicon nanowire has rotational symmetry, the field may not have the same circular symmetry and the polarized modes have either the H_x or H_y field as the dominant component. In this study, the $H^x{}_{mn}$ and $H^y{}_{mn}$ notation is used, where, in a way similar to that for the LP_{mn} modes, m identifies the approximate azimuthal variation and n identifies the radial variation, and, along with that, H^x or H^y identify the dominant **H**-field component, which is an important parameter to identify polarization states of the strongly confined modes. However, for each mode presented here, the two notations (LP_{mn} and E_{mn}/H_{mn}) are identified. Here, all the modes with the dominant H_x field have been considered, unless stated otherwise.

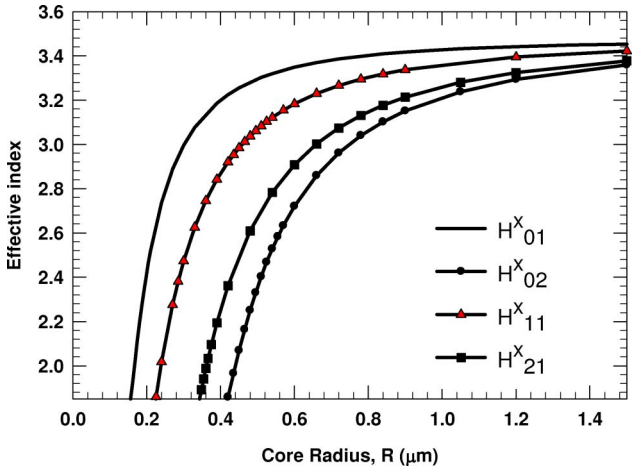

Fig. 1. Variations of the effective indices with the core radius.

The variation in effective index of the modes for an Si circular optical waveguide is studied as the radius of the waveguide decreases and it enters the nanowire regime. Figure 1 shows the variations of the effective indices with respect to the core radius for the y-polarized fundamental $H^x{}_{01}$ mode, where the effective index, n_e is defined as β/k_0, where β and k_0 are the propagation constant and wavenumber, respectively. For the circular optical waveguide, the vertically and horizontally polarized fundamental $H^x{}_{01}$ and $H^y{}_{01}$ modes of the waveguide (HE_{11} or LP_{01}) are degenerate, so the effective indices of the $H^y{}_{01}$ modes are not shown in Fig. 1. Further, Fig. 1 shows the higher order modes $H^x{}_{11}$ (HE_{01} or LP_{11}), $H^x{}_{21}$ (EH_{11} or LP_{21}), and $H^x{}_{02}$ (HE_{21} or LP_{02}). It can be noted that as the waveguide radius is increased, the effective index asymptotically approaches that of the silicon refractive index, when most of the optical power is confined in the silicon core. However, as the core radius is reduced, initially the effective indices of the modes reduce slowly, but these decrease rapidly as the modes approach their cutoff conditions. The single-mode operation of this silicon nanowire is possible for a value of the radius between 150 nm to 210 nm, at the operating wavelength of 1550 nm, which is further explained below using the effective area and confinement factors of each of the modes.

To suit various applications, the mode size or its effective area is an important modal parameter. Here, following the second moment of intensity distribution recommended by ISO Standard 11146, the effective area (A_{eff}) is used to evaluate this parameter. This value is related to σ_x and σ_y, the spot sizes along the X and Y axes, respectively, where the σ_x is defined as [20]:

$$\sigma_x{}^2 = \frac{4\int_S (x-\bar{x})^2 I(x,y)\,\mathrm{d}x\mathrm{d}y}{\int_S I(x,y)\,\mathrm{d}x\mathrm{d}y}, \qquad (1)$$

and σ_y follows a similar definition. Here, $I(x,y)$ is the power intensity profile and $\bar{x}$ is center of the modal

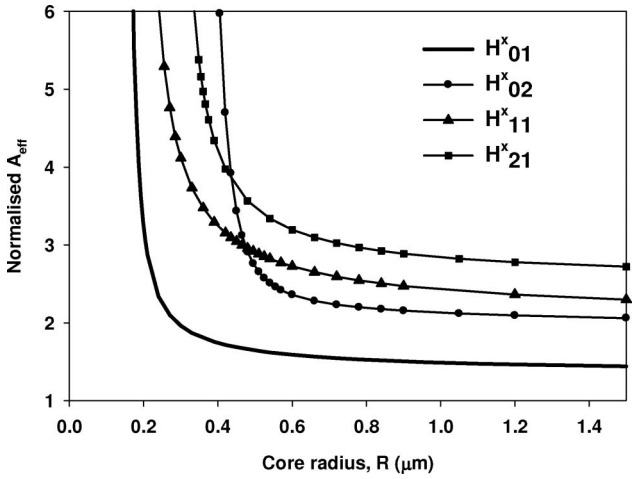

Fig. 2. Variations of the normalized A_{eff} with the core radius.

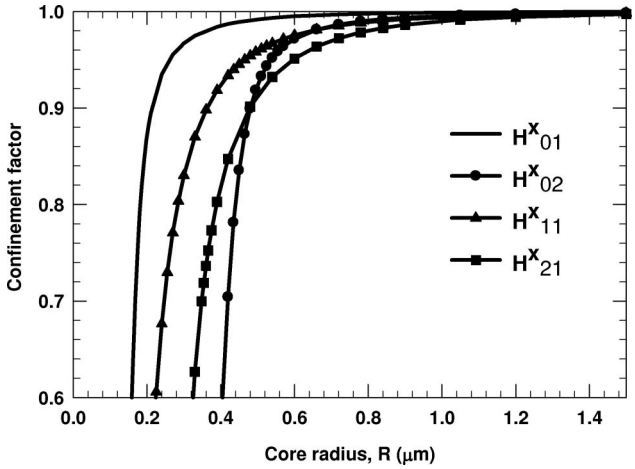

Fig. 3. Comparison of the confinement factors for the fundamental and higher order modes.

field. Using σ_x and σ_y, the effective area can be calculated as $A_{\text{eff}} = \pi^*(\sigma_x{}^2 + \sigma_y{}^2)/2$. However, often the normalized effective area ($\sigma_N = A_{\text{eff}}/R^2$) can be more useful, and Fig. 2 shows the normalized effective areas of the fundamental and higher order modes with respect to the core radius. The fundamental mode possesses a lower normalized effective area compared to the higher order modes, as this mode is more confined in the core. As the core radius is reduced, the corresponding normalized effective area, σ_N, increases slightly until the mode approaches the cutoff region. With the further reduction in R, its value of σ_N increases rapidly, as the mode spreads into the cladding. Variation of the effective area, A_{eff}, is not shown here, but its minimum value of 0.126 μm^2 at $R = 210$ nm was noted. Similarly, it can also be observed that the normalized effective areas increase for the $H^x{}_{02}$, $H^x{}_{11}$, and $H^x{}_{21}$ modes, as they approach their cutoff conditions. One feature that can be noticed is the $H^x{}_{02}$ mode with a higher radial variation ($n = 2$), and although it has a lower normalized effective area for a larger core radius, it approaches its cutoff before the $H^x{}_{11}$ or $H^x{}_{21}$ mode.

The variations of the confinement factor with the core radius for the fundamental and higher order modes are shown in Fig. 3. The confinement factor is defined as the fraction of the total power residing in the silicon core. In this case, the power has been calculated from the Poynting vector using all six components of the **E** and **H** fields. The rapid increase of the effective area and the rapid decrease of the confinement factor below $R = 200$ nm evidently shows that the fundamental mode is near the cutoff regime. Similarly, it can be observed from Fig. 3 that the cutoff radii for the $H^x{}_{01}$, $H^x{}_{11}$, $H^x{}_{21}$, and $H^x{}_{02}$ modes are around values of 160, 210, 320, and 400 nm, respectively, and these results also agree very well with the values seen in Fig. 1. It can also be observed that although the $H^x{}_{02}$ mode has a higher confinement factor (and a similarly smaller normalized effective area) for a higher core radius, this value reduces more rapidly as the radius reduces when compared to the other two modes: the $H^x{}_{11}$ and $H^x{}_{21}$ modes.

B. **H**-Field Mode Profile

It has been observed that when the radius of the core, R, is much smaller than the wavelength size, the fundamental mode may not be circular in shape [21], even though the nanowire structure is rotationally symmetric. For the $H^x{}_{01}$ mode, the x component of the **H** field is dominant and a two-dimensional (2D) contour of the H_x field is shown in Fig. 4 for the case where $R = 200$ nm. The maximum field intensity is at the center of the core and reduces monotonically along the radial direction. However, it can clearly be observed that the mode shape is not circular as the H_x field spreads more in the horizontal direction, resulting in a dumbbell-shaped profile. The detailed transverse variations of this field are discussed later and shown in Fig. 7.

The modes of an optical waveguide with a 2D confinement are not truly vertically or horizontally polarized, but hybrid in nature. Although, for the $H^x{}_{01}$ mode, the H_x field is dominant, the other two components also exist. The normalized H_y field contour is shown in Fig. 5, which clearly shows four peaks at

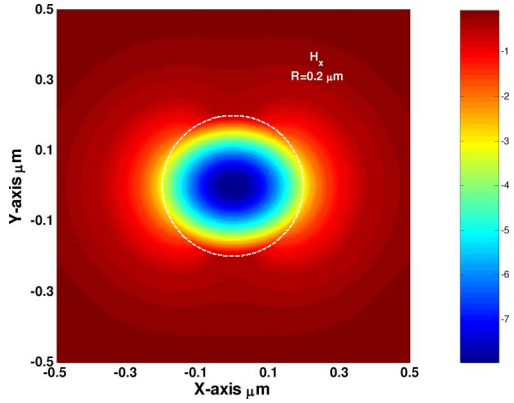

Fig. 4. (Color online) Contour plot of the H_x field for the quasi-$H^x{}_{01}$ mode.

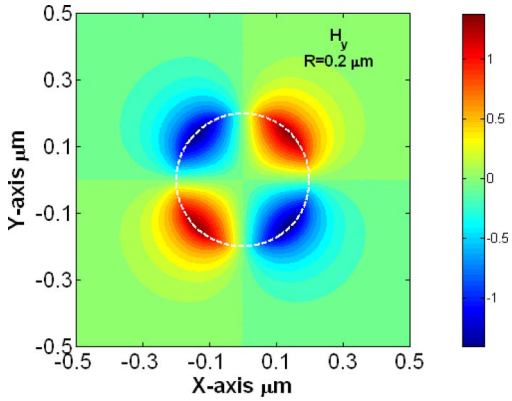

Fig. 5. (Color online) Contour plot of H_y field for the quasi-$H^x{}_{01}$ mode.

the silicon/silica interface at 90° intervals with alternate positive and negative signs. Its magnitude is smaller than the dominant H_x field, but not insignificant: for example, when $R = 200$ nm, its maximum value is about 18% of the maximum H_x field. Arising from the existing boundary conditions, its values along the X and Y axes are zero.

The normalized contour of the longitudinal H_z field is shown in Fig. 6. It can clearly be observed that its value along the Y axis is zero and it has two peaks along the X axis at the silicon/silica interfaces with positive and negative signs. Its peak value is significant, about 30% of the maximum H_x field, when $R = 200$ nm. It should be noted here that for a lossless waveguide, the axial H_z field is 90 ° out of phase with its transverse components.

The variations of the H_x and H_z fields along the axes are shown in Fig. 7 when $R = 200$ nm. For the fundamental $H^x{}_{01}$ mode, the magnetic and electric wall boundary conditions exist along the Y and X axes, respectively, and these have been exploited. Thus for this mode, although the H_y field exists, its value is zero along the X and Y axes, which is not shown here. Similarly, the H_z value is zero along the Y axis but nonzero along the X axis. It can be observed that the H_x field is better confined in the direction of the Y axis with its value only 5% of its peak

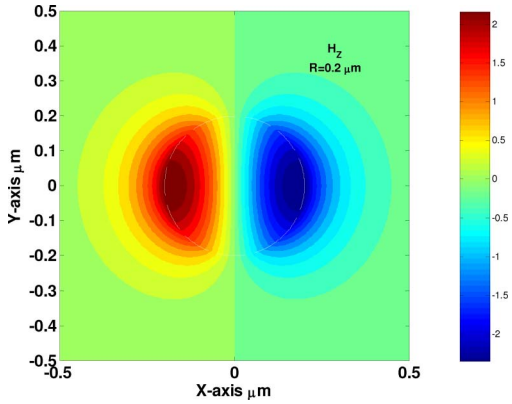

Fig. 6. (Color online) Contour plot of H_z field for the quasi-$H^x{}_{01}$ mode.

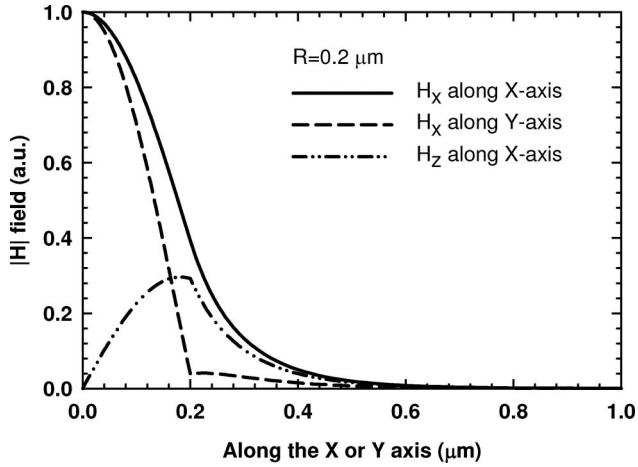

Fig. 7. Variation of the H fields along the X and Y axes for the quasi-$H^x{}_{01}$ mode.

at the silicon/silica interface at $y = R$. The variations of the H_x field along the Y axis are almost identical for all the R values considered here (when a normalized y/R is used), but this is not shown here. The H_x field varies more slowly along the X axis, and, in this case (where $R = 200$ nm), its value is about 40% of the maximum at the silicon/silica interface at $x = R$. As result, the spot-size diameter along the X axis is significantly larger compared to that along the Y axis for a smaller core radius. In this case, it can also be seen that the maximum value of the H_z field is at the silicon/silica interface, which is about 30% of the maximum H_x value. For most of the optical waveguides considered, the longitudinal fields are small, but as this field depends on the spatial variation of the dominant fields, for a submicron waveguide with a strong confinement (or stronger spatial variation), this quantity is expected to be higher.

Although the H_x field is continuous along both axes, E_y is only continuous along the X axis (and not continuous along the Y axis), and, as a result, the variations of the Poynting vector are not identical along the directions of X and Y axes, which is due to the overall boundary conditions for the E and H field components at the silicon/silica interfaces; this leads to an elliptical profile of the H_x field for the fundamental $H^x{}_{01}$ (LP_{01}) mode. A similar deviation from circular symmetry has been reported in vacuum-clad subwavelength optical fiber [22]. However, it should be noted that all the components of the **H** field are continuous across the dielectric interface in both the transverse directions. Similarly, it has been observed that the H_y field for the $H^y{}_{01}$ mode extends more along the direction of Y axis when compared to that of X axis direction, which is not shown here.

C. **E**-Field Profile

Once the magnetic field, **H**, is obtained from this **H**-field formulation [13], the corresponding **E** field can be calculated from $\nabla \times \mathbf{H}$ Maxwell's equations. For the $H^x{}_{mn}$ mode, the E_y field is dominant and this

component is directly related to the H_x field with an additional contribution from $\partial H_z/\partial_x$. The boundary condition at a dielectric interface demands that the tangential **E** field should be continuous. Similarly, it also requires that the normal **D** component should also be continuous, but this would make the normal component of the **E** field discontinuous at the dielectric interface.

The variations of the E_y field along the X and Y axes are shown in Fig. 8. Because E_y is the tangent to the silicon/silica interface at $x = R$, ($\hat{n} \| \hat{x}$, where $\hat{n}$ is the normal to the interface), the E_y field, shown here by a solid line, is continuous along the X axis. However, as the E_y field is normal to the interface at $y = R$, ($\hat{n} \| \hat{y}$), this field is discontinuous along the Y axis, as shown by a dashed curve. It should be noted that if the $\partial H_z/\partial_x$ contribution to the E_y is neglected, then E_y would also be discontinuous along the X axis, which would violate the continuity condition. Hence, for a waveguide with a strong index contrast, the H_z magnitude and its derivative need to be higher to satisfy the continuity condition. It can be noted that, although E_y reduces more quickly along the Y axis inside the core, it increases abruptly (by a ratio $\approx 3.4754^2/1.444^2$) in the silica cladding region. As a consequence, the magnitude of the E_y field in the low index cladding can be significantly higher than that in the core region. Here again, it is shown that the **E**-field variation along the directions of the X and Y axes are not identical, which gives rise to the asymmetry of the optical beam profile.

The E_x field is zero along the X and Y axes and is not shown here. The variation of the E_z field along the Y axis is also shown in Fig. 8, when $R = 200$ nm. It can be observed that E_z reaches its maximum value at the silicon/silica interface and then decays in the silica cladding region. The E_z field is zero along the X axis because of the electrical wall boundary condition for the $H^x{}_{01}$ mode along this symmetry axis. For a smaller radius, the maximum E_z field can be higher than that of the E_y field for the hybrid mode, $H^x{}_{01}$. By combining the transverse and longitudinal field components, a "flat-top" beam

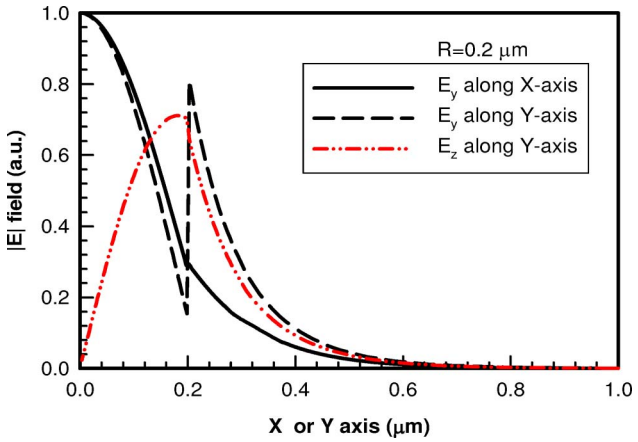

Fig. 8. (Color online) Variation of E fields along the X and Y axes for the quasi-$H^x{}_{01}$ mode.

with a spot size smaller than its diffraction limit may be obtained. This has importance for various applications, such as lithography, near-field microscopy, and optical data storage [23,24].

The prominent ellipticity of the $H^x{}_{01}$ modal field profile can be explained in terms of the electric field as follows: for a smaller core radius, the large discontinuity that occurs for the Ey field along the Y axis, combined with a large spatial variation of the longitudinal electric field, results in the elliptical profile of the mode $H^x{}_{01}$. It should be noted that for a circularly symmetric nanowire, the $H^y{}_{01}$ mode is degenerate with the $H^x{}_{01}$ mode by having identical propagation constants. However, its field profile, although similar, is rotated through 90 ° in space. Hence, the vertically and horizontally polarized field profile would be different for the two polarized modes. On the other hand, the superposition of $H^x{}_{01}$ and $H^y{}_{01}$ modes can yield a radially polarized HE_{11} mode.

Mode profiles for the higher order modes are not shown, but it was identified that they are fully vectorial with strong nondominant field components and they also possess ellipticity in their modal magnetic field profiles, when the radius of the core tends to be small.

D. Modal Hybridness

The modal hybridness is defined as the ratio of the maximum values of the nondominant to the dominant field components for a given mode. For the $H^x{}_{mn}$ mode, the hybridness can be defined as the ratio of the maximum values of the nondominant H_y or the H_z field over the dominant H_x field. Because of the presence of the nondominant component, the $H^x{}_{mn}$ mode is a quasi-vertically polarized mode. The modal hybridness increases with the index contrast, and this can be enhanced further by the presence of waveguide asymmetry. In a low index contrast waveguide, such as silica optical fiber, hybridness is very small (less than 0.001). However, it is expected that hybridness would be higher in a high index contrast silicon nanowire. The variations of the modal hybridness, H_y/H_x and H_z/H_x, with the core radius, R, are shown in Fig. 9. It can be observed that, as the core radius is reduced below the value of λ, the hybridness increases vary rapidly. At $R = 200$ nm, the modal hybridness reaches a value that is significantly higher compared to that when the core is as large as $R = 1.5$ μm. Modal hybridness is a key modal property in polarization issues such as polarization cross talk or polarization mode dispersion. Polarization conversion can take place due to the interaction of the dominant and nondominant components of the $H^x{}_{01}$ and $H^y{}_{01}$ modes [25], and this is an important parameter for polarization cross talk studies [26]. Because of the large values of E_y and E_z, which are in phase and $\pi/2$ out of phase with the dominant E_x component, respectively, the total **E** field would be elliptically polarized.

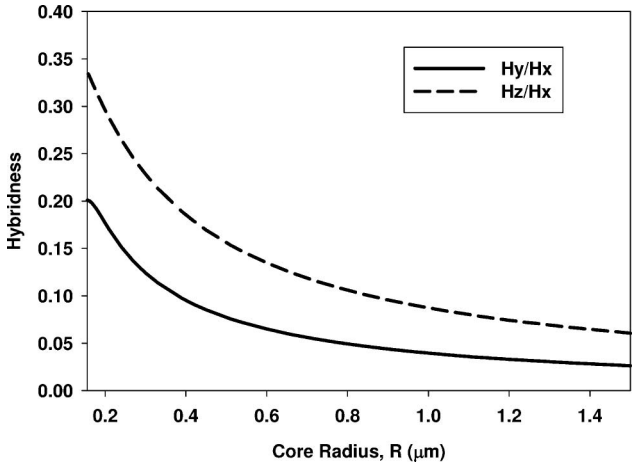

Fig. 9. Variations of the H_y/H_x and H_z/H_x with core radius, R, for the quasi-$H^x{}_{01}$ mode.

E. Poynting Vector

The quasi-vertically or -horizontally polarized modes supported by a nanowire optical waveguide are strongly hybrid in nature, as discussed in the previous section and contain all six components of the **E** and **H** fields. In such a case, the optical power should be calculated from the Poynting vector (S_z) using the full-vectorial **E** and **H** fields [27] rather than simply from its $\mathbf{E}^2$ profile. It has been shown in Figs. 7 and 8 that both the dominant H_x and E_y fields are not circularly symmetric. The Z-axis component of the Poynting vector (**S**), calculated from the total **E** and **H**-fields, is also not circularly symmetric, as shown in Fig. 10 for the case where $R = 200$ nm. This S_z is extended more along the direction of the X axis but is continuous and decreases monotonically. On the other hand, initially S_z reduces more rapidly along the Y axis inside the core and then has a small discontinuity peak (not clearly visible in the contour plot) at the silicon/silica interface. The outline of the silicon core is shown by a dashed circle.

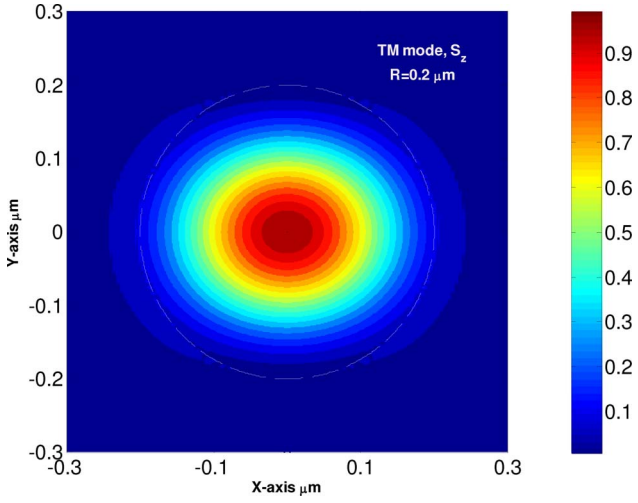

Fig. 10. (Color online) Contour plot of the S_z for the quasi-$H^x{}_{01}$ mode.

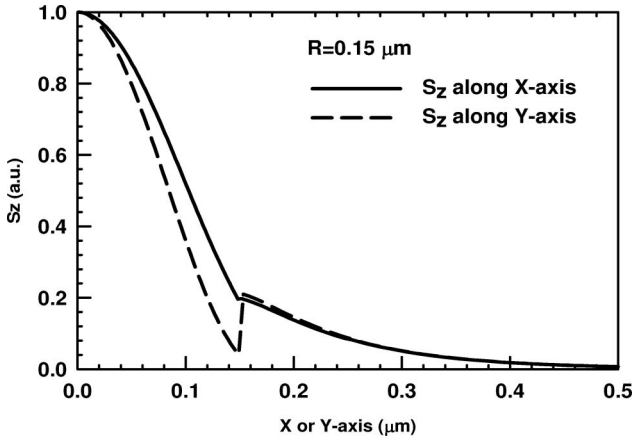

Fig. 11. Variation of S_z for the quasi-$H^x{}_{01}$ mode along the X and Y axes.

As R is reduced further, the E_y field can be higher in the low index cladding region. The more detailed transverse variation of S_z is shown in Fig. 11 when $R = 150$ nm. The variation of S_z along the X axis is shown by a solid curve, which illustrates a monotonic reduction along the direction of the X axis. On the other hand, initially S_z reduces more rapidly along the Y axis inside the core region, but it is, however, accompanied by a large increase at the silicon/silica interface. For this reason, it should be noted that for an even smaller core radius, the value of S_z can extend more along the Y axis direction. The variation of the S_z profile for the quasi-horizontally polarized $H^y{}_{01}$ mode (not shown here) is almost identical to that of the $H^x{}_{01}$ mode shown in Figs. 10 and 11, but rotated by 90 ° in space.

F. Modal Asymmetry

It has been shown here that for a smaller radius, both the **E** and **H** fields and also the Poynting vector are not rotationally symmetric. To quantify this feature, the variations of the spot size σ_x and σ_y for the $H^x{}_{01}$ mode are shown in Fig. 12 (right-hand axis) by the triangular symbol and circular symbol, respectively. It can be observed that as the core radius is reduced, the spot-size values are also reduced. Further, for a

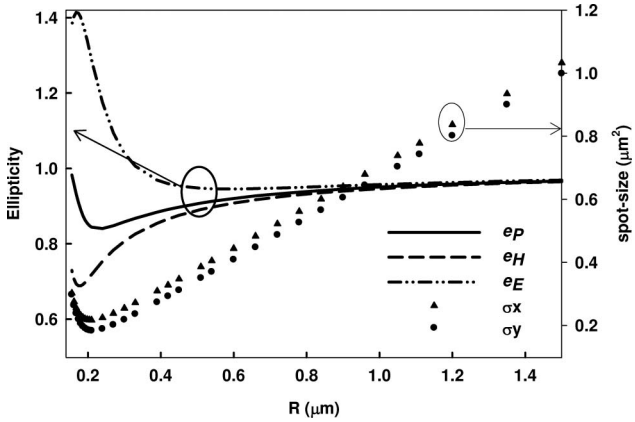

Fig. 12. Effective area and the ellipticity for the quasi-$H^x{}_{01}$ mode.

larger core radius, R, the spot sizes, σ_x and σ_y, shown are nearly the same. However, as the core radius, R, is reduced, σ_x becomes higher than σ_y and the geometric difference increases progressively. The ellipticity, e_P, obtained from the ratio σ_y to σ_x is shown by a solid curve (using the left-hand side axis). It can be noted that for a higher core radius, $e_P \sim 1$, and this value reduces to 0.85 before the $H^x{}_{01}$ mode approaches its cutoff.

It can be noted in Fig. 12, for a very small core radius, the asymmetry improves slightly, and this is due to an increase of the value of S_z in the silica cladding along the Y axis. Further, it can seen that the Poynting vector profile for $R = 150$ nm along the X and Y axes looks almost identical in the cladding in Fig. 11, where this is not true for $R = 200$ nm [Fig. 10].

A similar approach of evaluating the asymmetry can be applied on the intensity of the magnetic field $|H_x|^2$ and on the intensity of the electric field $|E_y|^2$. Equation (1) had been used to evaluate the second moment of the intensity distribution of the magnetic and that of the electric fields. Following that, the ellipticity of the magnetic field intensity (e_H) has been evaluated using the ratio of the spot size along the Y axis ($\sigma^H{}_y$) to that along the X axis ($\sigma^H{}_x$) as follows:

$$e_H = \sigma^H{}_y / \sigma^H{}_x. \tag{2}$$

Similarly, ellipticity of the electric field (e_E) has been evaluated using the ratio of the spot size along the Y axis ($\sigma^E{}_y$) to that of along the X axis ($\sigma^E{}_x$) as follows:

$$e_E = \sigma^E{}_y / \sigma^E{}_x. \tag{3}$$

Figure 12 shows the ellipticity calculated for the intensity of the magnetic and electric fields. When the core is small, it can be seen that e_H reduces to ~0.70, showing the prominent deviation from the circular symmetry. The ellipticity of the electric field intensity, e_H is nearly 1 when the core is larger and the power in the silica cladding is very small. However, as the core diameter is progressively reduced, the peak of the electric field in the silica region along the Y axis starts to increase, causing the ellipticity e_E to rise above unity.

G. Dispersion

Controlling light propagation by tailoring the waveguide dispersion is widely used, particularly for nonlinear devices, such as Raman amplification, four-wave mixing, and supercontinuum generation. It is known that deeply scaled waveguides, with smaller physical dimensions compared to the operating wavelength, deviate further from the material dispersion curve, and these can be engineered for various specific applications. The dispersion profiles for five different core diameters are shown in Fig. 13. The Sellmeier equations for silica [19] and silicon [9] have been used to obtain their wavelength-dependent refractive index values. The GVD values,

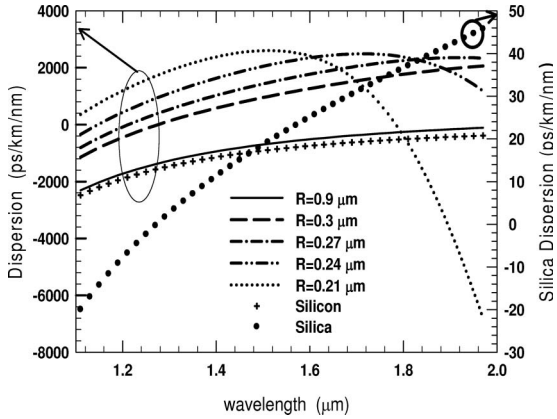

Fig. 13. GVD profiles for five different core diameters for silicon core with silica cladding.

D, are obtained from the spectral dependence of the effective indices, as given below [19]:

$$D = -\frac{\lambda}{c}\frac{d^2 n_{\text{eff}}}{d\lambda^2}. \tag{4}$$

The material dispersion curve for silicon is shown by "+" points. The material dispersion of silica (corresponding to the scale on the right-hand axis) is shown using dot symbols. This value is very small compared to that for silicon, and it crosses the zero position at around 1.29 μm.

When the core radius is as large as $R = 0.9$ μm, most of the power resides inside the core with a confinement factor greater than 0.99 and, hence, the dispersion curve is very similar to that of material dispersion of silicon. However, when $R = 0.3$ μm, for the smaller wavelength value, the field remains well confined in the silicon core. The waveguide dispersion shows a similar behavior to the material dispersion of silicon until the operating wavelength reaches values around 1.2 μm–1.3 μm. However, as the wavelength is increased further, the modal field spreads considerably into the silica cladding. As mentioned earlier, the profile deviates from a circular shape and the E_y field of the $H^x{}_{01}$ mode peaks near the interface in the silica cladding region. In this case, this peak value in silica cladding ($E^p{}_{\text{silica}}$) is less than the maximum value of the E_y field at the center of the core ($E^p{}_{\text{silicon}}$). The ratio of $E^p{}_{\text{silica}}/E^p{}_{\text{silicon}}$ increases as the wavelength is increased. With the electric field starting to penetrate considerably into the silica region, the effective index tends to reduce at a faster rate with the wavelength increase. As a result, a zero dispersion can be seen around $\lambda = 1.29$ μm for $R = 0.3$ μm. The zero dispersion is blueshifted with the decrease of the core radius. For still-smaller core radius values, the accumulation of power in the silica tends to be large, so that, at a particular higher value of wavelength, the dispersion reaches the maximum value. Thereafter, further increase in the wavelength still results in the reduction of the effective index, leading toward the cladding refractive index, but at a slower rate.

This results in the change of slope in the higher wavelength region when the core radius is smaller, as seen for $R = 0.27$–$0.21\ \mu$m. As this phenomena is blueshifted, as R decreases, a second zero dispersion is achieved for $R = 0.21\ \mu$m.

Most of the optical power and electric field intensity resides in the silicon core at the lower wavelength regime, when $R \approx 0.2\ \mu$m. However, at the higher wavelengths, most of the electric field intensity is in the silica. Because the induced electric susceptibility is proportional to the electric field, optical nonlinearity at a higher wavelength could be determined by the interaction of the light with both the silicon and in silica.

3. Conclusion

It has been shown here that for an Si nanowire with a small radius, the electric and magnetic modes are fully vectorial, with all the six components present. Hence, to obtain the modal solutions of such a waveguide, it is essential to use a fully vectorial formulation. It has also been indicated that the **H**-field components are continuous across the dielectric interfaces but not the **E** field. It should be noted that, if, instead of the **H**-field formulation, an **E**-field formulation is used, this may wrongly force the continuity of the **E** field across the dielectric interface and introduce a significant error, particularly for a high index contrast optical waveguide. Hence, an **E**-field-based formulation would not be suitable unless an additional integral is incorporated at the interfaces, which may be tedious and increase the computational overhead/complexity, if this interface has an arbitrary profile or even a simple regular circular shape, as in the case of a nanowire.

It has also been shown the modal field is not symmetric, even though the structure is rotationally symmetric, and, hence, in the analysis such symmetry should not be used or enforced, as is often used in field expansion techniques. Hence, it should be noted that any numerical approach that considers circularly symmetric fields and enforces nonexisting circular symmetry of the field component can produce erroneous results when the core radius is small.

Furthermore, it has been indicated that all the field components do not reduce monotonically along the radial directions, with a strong **E** field in the cladding region. It is shown that the field variation is not Gaussian in shape. In that case, the spot-size calculation from a local field value may produce ambiguous results, and for that reason, an integral form has been used to calculate the effective area of the modes.

The modal asymmetry of the higher order modes have been identified as well, but this is not shown here. Such asymmetry can have an impact on sensor-based devices that may be developed and on the coupling between two nanowires. Similarly, it has been observed that the H_y field for the $H^y{}_{01}$ mode is also elliptical with its height larger than its width. However, the two modes, $H^y{}_{01}$ and $H^x{}_{01}$, are degenerate with identical propagation constants. Although the polarized modes do not have circular symmetry, the superposition of the degenerate $H^x{}_{01}$ and $H^y{}_{01}$ can, however, produce a radially polarized HE_{11} mode.

It has further been shown in this work that the modes in such nanowires with strong index contrast have hybridness or show the presence of the nondominant orthogonal polarization (for example, H_x component is nonzero for a H_y-dominant mode). The existence of these nondominant transverse components may have a strong effect on the polarization cross talk in these devices, particularly in the presence of any manufacturing deformity that may be introduced. On the other hand, the existence of larger longitudinal field components can also be exploited for various novel applications, such as beam shaping or atom trapping. It has also been indicated that the dispersion properties can be strongly controlled when the waveguide dimensions are small for various linear and nonlinear applications. However, a rigorous full-vectorial approach, which can correctly represent the field continuity condition, must be used to optimize the properties of nanowire-based devices.

References

1. J. L. Liu, Y. Shi, F. Wang, Y. Lu, S. L. Gu, R. Zhang, and Y. D. Zheng, "Study of dry oxidation of triangle-shaped silicon nanostructure," Appl. Phys. Lett. **69**, 1761–1763 (1996).
2. M. Lipson, "Guiding, modulating, and emitting light on silicon- challenges and opportunities," J. Lightwave Technol. **23**, 4222–4238 (2005).
3. B. G. Lee, X. Chen, A. Biberman, X. Liu, I.-W. Hsieh, C.-Y. Chou, J. I. Dadap, F. Xia, W. M. J. Green, L. Sekaric, Y. A. Vlasov, R. M. Osgood, and K. Bergman, "Ultrahigh-bandwidth silicon photonic nanowire waveguides for on-chip networks," IEEE Photon. Technol. Lett. **20**, 398–400 (2008).
4. V. Yurii, O'Boyle Martin, F. H. Hendrik, and J. McNab Sharee, "Active control of slow light on a chip with photonic crystal waveguides," Nature **438**, 65–69 (2005).
5. F. L. Kien, V. I. Balykin, and K. Hakuta, "Atom trap and waveguide using a two-color evanescent light field around a subwavelength-diameter optical fiber," Phys. Rev. A **70**, 063403 (2004).
6. J. Y. Lou, L. M. Tong, and Z. Z. Ye, "Modeling of silica nanowires for optical sensing," Opt. Express **13**, 2135–2140 (2005).
7. Ansheng Liu, Ling Liao, Doron Rubin, Hat Nguyen, Berkehan Ciftcioglu, Yoel Chetrit, Nahum Izhaky, and Mario Paniccia, "High-speed optical modulation based on carrier depletion in a silicon waveguide," Opt. Express **15**, 660–668 (2007).
8. W. H. P. Pernice, M. Lo, and H. X. Tang, "Theoretical investigation of the transverse optical force between a silicon nanowire waveguide and a substrate," Opt. Express **17**, 1806–1816 (2009).
9. C. Turner, C. Manolatou, B. S. Schmidt, M. Lipson, M. A. Foster, J. E. Sharping, and A. L. Gaeta, "Tailored anomalous group-velocity dispersion in silicon channel waveguides," Opt. Express **14**, 4357–4362 (2006).
10. E. Dulkeith, F. Xia, L. Schares, W. M. J. Green, and Y. A. Vlasov, "Group index and group velocity dispersion in silicon-on-insulator photonic wires," Opt. Express **14**, 3853–3863 (2006).
11. I.-W. Hsieh, X. Chen, X. Liu, J. I. Ddap, N. C. Panoiu, C.-Y. Chou, F. Xia, W. M. Green, Y. A. Vlasov, and R. M. Osgood, Jr., "Supercontinuum generation in silicon photonic wires," Opt. Express **15**, 15242–15249 (2007).

12. L. Yin, Q. Lin, and G. P. Agrawal, "Soliton fission and supercontinuum generation in silicon waveguides," Opt. Lett. **32**, 391–393 (2007).
13. B. M. A. Rahman and J. B. Davies, "Finite-element solution of integrated optical waveguide," J. Lightwave Technol. **2**, 682–688 (1984).
14. G. Brambilla, V. Finazzi, and D. J. Richardson, "Ultra-low-loss optical fiber nanotapers," Opt. Express **12**, 2258–2263 (2004).
15. S. G. Leon-Saval, T. A. Birks, W. J. Wadsworth, and P. St. J. Russel, "Supercontinuum generation in submicron fiber waveguides," Opt. Express **12**, 2864–2869 (2004).
16. L. Tong, L. Hu, J. Zhang, J. Qiu, Q. Yang, J. Lou, Y. Shen, J. He, and Z. Ye, "Photonic nanowires directly drawn from bulk glasses," Opt. Express **14**, 82–87 (2006).
17. Y. K. Lize, E. Magi, V. Taeed, J. Bolger, P. Steinvurzel, and B. Eggleton, "Micostructured optical fiber photonic wires with subwavelength core diameter," Opt. Express **12**, 3209–3217 (2004).
18. L. Tong, J. Lou, and E. Mazur, "Single-mode guiding properties of subwavelength-diameter silica and silicon wire waveguide," Opt. Express **12**, 1025–1035 (2004).
19. G. P. Agrawal, *Nonlinear Fiber Optics*, 3rd ed. (Academic, 2001).
20. ISO 11146, Laser and laser related equipment—Test methods for laser beam widths, divergence and beam propagation ratios, International Organization for Standardization, Geneva, Switzerland, 2005.
21. M. Koshiba and Y. Tsuji, "Curvilinear hybrid edge/nodal elements with triangular shape for guided-wave problems," J. Lightwave Technol. **18**, 737–743 (2000).
22. F. L. Kien, J. Q. Liang, K. Hakuta, and V. I. Balykin, "Field intensity distributions and polarization orientations in a vacuum-clad subwavelength-diameter optical fiber," Opt. Commun. **242**, 445–455 (2004).
23. J. B. Driscoll, X. Liu, S. Yasseri, I. Hsieh, J. I. Dadap, and R. M. Osgood, Jr., "Large longitudinal electric fields (E_z) in silicon nanowire waveguides," Opt. Express **17**, 2797–2804 (2009).
24. Q. Zhan and J. R. Lager, "Focus shaping using cylindrical vector beams," Opt. Express **10**, 324–331 (2002).
25. B. M. A. Rahman, N. Somasiri, and M. Windmann, "Polarization crosstalk in high index contrast planar silica waveguides," IEEE Photon. Technol. Lett. **14**, 1109–1111 (2002).
26. E. D. Finlayson, J. M. Heaton, B. M. A. Rahman, and S. S. A. Obayya, "Polarization conversion in passive deep-etched GaAs/AlGaAs waveguides," J. Lightwave Technol. **24**, 1425–1432 (2006).
27. J. T. Robinson, K. Preston, O. Painter, and M. Lipson, "First-principle derivation of gain in high-index-contrast waveguides," Opt. Express **16**, 16659–16669 (2008).